Catalysis Today 160 (2011) 191–197

Contents lists available at ScienceDirect

Catalysis Today

journal homepage: www.elsevier.com/locate/cattod

Copper promotion of high temperature shift

John S. Coleman, Mang Zhang, Rainee M. VanNatter, Carl R.F. Lund*

Department of Chemical and Biological Engineering, University at Buffalo, SUNY, Buffalo, NY 14260, United States

ARTICLE INFO

Article history:
Available online 9 June 2010

Keywords:
Water-gas shift kinetics
Water-gas shift mechanism
Copper water-gas shift promoter

ABSTRACT

A four-step, redox kinetic mechanism provides an accurate description of the rate of water-gas shift over ferrochrome catalysts. When the heats of formation of the surface intermediates in the model are decreased by only 10 kJ mol^{-1}, as might be expected when copper cations substitute for iron cations in the oxide catalyst, the model predicts increased activity and decreased inhibition by CO_2. Experimental measurements using copper-promoted ferrochrome catalysts confirm these predictions. Furthermore, with small changes in most of the thermodynamic parameters, the same four-step, redox kinetic mechanism accurately models the rate of water-gas shift over the promoted catalyst. A four-step mechanism involving a formate intermediate also fits the experimental data for ferrochrome and for copper-promoted ferrochrome. The changes in the thermodynamic parameters for the formate mechanism are greater than those for the redox mechanism, but still within a range that can be ascribed to substitution of copper cations for iron cations in the ferrochrome catalyst. The results show that the formation of metallic copper is not necessary to explain the effect of copper promotion for either redox or associative mechanisms.

1. Introduction

Water-gas shift, Eq. (1), is a well-studied and highly optimized commercial process that has been practiced for many decades. It is often employed in the purification of hydrogen that contains carbon monoxide. The reaction is exothermic and reversible; as the temperature increases, the equilibrium conversion decreases. For this reason, shift is often practiced in stages, with initial high temperature stages followed by lower temperature final stages. The best known commercial high temperature water-gas shift (HTWGS) catalysts are ferrochrome based materials that have an operating range of ca. 600–750 K [1].

$$CO + H_2O \rightarrow CO_2 + H_2 \quad (1)$$

The forward rate of reaction over these catalysts is inhibited by the CO_2 product [2–7]. Bohlbro conducted an extensive study of the kinetics of high temperature water-gas shift over iron-chrome oxide catalysts [1–6]. He used a power-law rate expression to model the kinetics, and found Eq. (2) to best describe his atmospheric pressure data. In Eq. (2) $k_{0,1}$ is the pre-exponential factor for the reaction (1) rate coefficient, E_1 is the corresponding activation energy, K_1 is the equilibrium constant for reaction (1), R is the gas constant, T is the temperature and P_i is the partial pressure of species i. The inhibition effect is clearly reflected in the negative reaction order with respect to CO_2. It is important to realize that CO_2 causes a decrease in the *forward* rate of reaction. CO_2 inhibition is *not* a consequence of approaching equilibrium (the term in parentheses in Eq. (2) accounts for the approach to equilibrium). Bohlbro reported the apparent activation energy for a commercial ferrochrome catalyst to be 115 kJ mol^{-1}.

$$r_1 = k_{0,1} e^{(-E_1/RT)} P_{CO}^{0.9} P_{H_2O}^{0.25} P_{CO_2}^{-0.6} \left(1 - \frac{P_{CO_2} P_{H_2}}{K_1 P_{CO} P_{H_2O}}\right) \quad (2)$$

The mechanism of water-gas shift over the high temperature, iron oxide-based catalyst still is not firmly established, but a redox type of mechanism appears to be most widely accepted [8–16]. The evidence supporting a redox mechanism includes agreement between the shift rate and the rates of catalyst oxidation and reduction [10,11,13], a common catalyst oxidation state at conditions where these rates are equal [13] and the effect of oxidizing promoters upon the catalytic activity [14]. Associative mechanisms, such as those involving formate intermediates, have also been proposed [12,17–20]. Evidence used in support of associative mechanisms includes spectroscopic detection of formate during reaction [20], chemical trapping of formic acid via quenching [12] and isotopic study of the stoichiometric number [17–19].

It is well established [8,21–25] that the chromium cations that substitute within the iron oxide lattice to form a ferrochrome catalyst serve to stabilize the active surface area without changing the specific rate of reaction, the reaction orders or the apparent activation energy. Copper also is used to promote commercial iron oxide HTWGS catalysts. It is beneficial when the ratio of steam to CO in the feed is low because it prevents the formation of undesirable side products like methane [26,27]. Andreev et al. [28] observed

* Corresponding author. Tel.: +1 716 645 1180; fax: +1 716 645 3822.
E-mail address: lund@buffalo.edu (C.R.F. Lund).

0920-5861/$ – see front matter © 2010 Elsevier B.V. All rights reserved.
doi:10.1016/j.cattod.2010.05.006

nearly equal rates for Fe_3O_4 and Fe_2CuO_4 except that the copper-containing catalyst was more active at temperatures below ca. 350 °C. Similarly, the addition of 5% CuO to a ferrochrome catalyst resulted in nearly equal activities: the unpromoted material was slightly more active above 400 °C while the copper-promoted material was slightly more active below 400 °C. The addition of copper has been reported to reduce the apparent activation energy (i.e. increase catalytic activity) with no effect upon the reaction rate orders with respect to CO and H_2O [27,29]. It has recently been suggested that copper has two roles as a promoter: copper cations within the oxide stabilize that structure while surface copper provides new active sites [30,31].

Copper cations can replace iron cations in the spinel structure of iron oxide catalysts [24]. It has been suggested that the promotional effects of copper are due to this oxide substitution [24,27,29]. Alternatively, the promotional effect has been attributed to the generation of metallic copper sites under reaction conditions [32–35]. While separate metallic copper crystallites have been observed in some studies, they were not detected in others [24,27]. During temperature programming, the reduction of the copper in promoted iron oxide catalysts begins at higher temperatures than observed with pure copper oxide, indicating its incorporation in or stabilization by the iron oxide [34]. At the same time, the presence of the copper component leads to lower onset temperatures for the reduction of the iron oxide [33].

Recent computational chemistry results indicate that, for metallic copper, the predominant mechanism involves carboxyl intermediates [36]. The reaction rate over metallic copper is first order in both steam and carbon monoxide, it is negative one-half order in both hydrogen and carbon dioxide and the apparent activation energy is of the order of 70 kJ mol^{-1}. This differs significantly from Eq. (2). In the case of iron oxides containing substitutional copper cations, computational chemistry suggests that copper cations located within the oxide but near the surface, decrease the strength of bonding of water-gas shift intermediates to the surface by less than 20 kJ mol^{-1} [37]. In contrast, copper cations in surface sites decrease the bond strength by 60–80 kJ mol^{-1} [37].

2. Methods

A base ferrochrome catalyst was prepared by precipitation from an aqueous solution of ferric and chromium sulfate. An appropriate amount of chromium(III) sulfate hydrate ($Cr_2(SO_4)_3{\cdot}H_2O$) was first dissolved in 200 mL distilled water (with one drop of sulfuric acid to prevent $Cr(OH)_3$ precipitation). The solution was placed on a heated stir plate with magnetic stirring; the nominal solution temperature was 70–80 °C. After pouring the upper clear blue solution into a 1000 mL beaker, 200 mL of additional distilled water was added. Due to the low solubility of $Cr_2(SO_4)_3$, these steps were repeated several times until all solid $Cr_2(SO_4)_3$ disappeared and a homogenous solution formed. After that, a weighed amount of iron(III) sulfate hydrate ($Fe_2(SO_4)_3{\cdot}xH_2O$) was dissolved in the above Cr^{3+} solution. Excess ammonium hydroxide was added drop-wise to the solution to precipitate an oxide while stirring vigorously. After the precipitate was aged overnight, distilled water was used to rinse it until no SO_4^{2-} ion could be detected in the wash solution by $BaCl_2$. The resulting precipitate was filtered to remove water, and the paste was put into a muffle furnace, heated at 300 °C overnight, ground to powder, calcined at 600 °C for 4 h, cooled, sieved, and stored. This base catalyst will be denoted as FeCr10, signifying the nominal weight ratio of the chromium to iron.

A series of Cu-promoted ferrochrome catalysts was prepared by mixing FeCr10 and copper nitrate in ethanol and evaporating the solvent. Specifically, an appropriate amount of copper(II) nitrate hemipentahydrate ($Cu(NO_3)_2{\cdot}(5/2)H_2O$) was put into a 100 mL volumetric flask and ethyl alcohol was added to make 100 mL of a copper ethanol standard solution. According to the desired copper loading, a weighed amount of FeCr10 catalyst was put into a crucible and copper ethanol standard solution was transferred into the crucible by pipette with additional pure alcohol to help mixing. This paste was put into a furnace and heated at 80 °C overnight, until the ethanol vaporized. After that, the paste was heated at 200 °C for 2 h to decompose the copper nitrate. After being ground, the catalyst powder was calcined at 600 °C for 4 h and then cooled, sieved and stored. The copper-promoted catalysts will be referred to as #%CuFeCr10, where # is the nominal weight percentage of copper in the final oxide catalyst. Catalysts 0.1%CuFeCr10, 1%CuFeCr10, 5%CuFeCr10, 10%CuFeCr10, and 20%CuFeCr10 were synthesized in this manner.

The chemical composition of the prepared catalyst was measured by Galbraith Laboratory, Inc. using ICP-OES (Inductively Coupled Plasma Optical Emission Spectroscopy). Surface areas were determined by the BET method, using a Micromeritics ASAP 2010 instrument and adsorption isotherm data between 0.07 and 0.20 relative pressure. Powder X-ray diffraction (XRD) patterns were measured with a Siemens D500 X-ray diffractometer, using Cu Kα radiation. The diffraction data were recorded for 2θ angles between 1° and 80°, with a resolution of 0.02°.

For kinetic measurements, CO (Cryogenic Supply, CP grade), CO_2 (Cryogenic, Bone Dry Grade), H_2 (Cryogenic, Pre-purified Grade) and Ar (Cryogenic, High Purity Grade) were fed from cylinders using Omega FMA-A2402 mass flow controllers. The gases were mixed in a common manifold that flowed to a packed bed of 100 mesh glass beads (Alltech) housed in a tube furnace with temperature control. Water was also fed to this packed bed from an ISCO Series D syringe pump and controller. Beyond this point all lines were heat traced to prevent the condensation of water. The reactor consisted of a vertically oriented quartz tube with a 6 mm outside diameter, a 1 mm wall thickness and a 560 mm length. A thermocouple entered the tube coaxially from the top and extended into the catalyst bed, and a second one entered from the bottom, extending into the reactor tube below the catalyst bed. These thermocouples were used to monitor the bed and reactor temperatures. The reactor was positioned within a split tube furnace (Lindberg type 54231). The thermocouple built into the furnace was used to control the temperature via an Omega CN9000A temperature controller. The catalyst bed rested upon glass wool, centered within the furnace. A backpressure regulator was used to set reactor pressure. No evidence of external heat or mass transfer was observed upon varying the WHSV to as high as 52,800 h^{-1}. While there was a small temperature gradient within the bed, it was caused by the furnace since it persisted when inert gas flow replaced reactant flow. The conversion was far less than equilibrium in all experiments. Experimental tests indicated that transport limitations could safely be ignored in the analysis of the reactor data.

A sampling valve permitted analysis of the gas before and after the reactor using an SRI 8610 gas chromatograph. A GC column packed with 80–100 mesh Porapak QS (Alltech) was used to separate the gases, which were detected using a thermal conductivity detector. CO and CO_2 were then hydrogenated to methane and also detected using a flame ionization detector. A personal computer running PeakSimple II (SRI) was used for data collection and analysis. Typically, ca. 0.1 g of catalyst was packed in the reactor and the reactor temperature, pressure and feed composition were set to desired levels. The system was allowed to attain steady state, after which the inlet and outlet compositions were measured. At least three sets of inlet and outlet analyses were used to ensure the system had indeed reached steady state. The inlet composition was determined from the full gas chromatographic analysis of the inlet gas stream. The CO conversion, *f*, was calculated using Eq. (3) and the inlet (superscript 0) and outlet (no superscript) molar ratios of

Table 1
Rate expressions for mechanistic modeling.

Rate expressions	$r_4 = k_4 P_{H_2O}\theta_v \left\{1 - \frac{\theta_{HOH}}{K_4 P_{H_2O}\theta_v}\right\}$
	$r_5 = k_5 \theta_{HOH} \left\{1 - \frac{P_{H_2}\theta_O}{K_5\theta_{HOH}}\right\}$
	$r_6 = k_6 P_{CO}\theta_O \left\{1 - \frac{\theta_{OCO}}{K_6 P_{CO}\theta_O}\right\}$
	$r_7 = k_7 \theta_{OCO} \left\{1 - \frac{P_{CO_2}\theta_v}{K_7\theta_{OCO}}\right\}$
Partial pressures	$P_i = \frac{n_i}{n_{CO}+n_{H_2O}+n_{CO_2}+n_{H_2}+n_{inert\ diluent}} P_{total}$

CO_2 to CO, as measured gas chromatographically.

$$f = \frac{\left(\frac{n_{CO_2}}{n_{CO}}\right) - \left(\frac{n^0_{CO_2}}{n^0_{CO}}\right)}{1 + \left(\frac{n_{CO_2}}{n_{CO}}\right)} \quad (3)$$

The kinetic data were analyzed in terms of the mechanistic kinetic model given in Eqs. (4)–(7), which was formulated in the same manner as described previously [38]. In these equations, the asterisk (*) symbol represents a surface cation and the oxygen anions surrounding it. Hence, H–*–OH corresponds to a hydrogen atom adsorbed on an oxygen anion (essentially forming a hydroxyl group) along with a hydroxyl group adsorbed on the cation. The rate expressions for the mechanistic steps are presented in Table 1. Expressions for the rate coefficients and equilibrium constants appearing in Table 1 are given in Table 2. Assuming zero degrees of translational freedom for all surface species and activated complexes, the entropies of activation (superscripted double daggers) and the entropies of reaction (superscripted zeroes) appearing in Table 2 were approximated to be equal to the corresponding change in translational entropy. The enthalpies of activation appearing in Table 2 were treated as unknown parameters whose values were determined by fitting the kinetic model to experimental data. The enthalpies of reaction appearing in Table 2 were calculated from the standard enthalpies of formation of the species participating in the corresponding mechanistic step. For gas phase species, these enthalpies of formation were computed, as a function of temperature, using the Shomate equation and data from the NIST Chemistry Webbook [39]. For surface phase species, the enthalpies of formation were set equal to a gas phase value that was computed in the same way plus an additional, constant "heat of localization" that accounted for the enthalpy change associated with bonding the species to the surface. These enthalpies of localization were treated as additional unknown parameters that needed to be determined by fitting the kinetic model to experimental data. With this formulation, the mechanistic kinetic model contained seven unknown parameters: four enthalpies of activation and three enthalpies of localization ($\Delta H^\circ_{loc,HOH}$, $\Delta H^\circ_{loc,0}$, $\Delta H^\circ_{loc,OCO}$, $\Delta H^\ddagger_4$, $\Delta H^\ddagger_5$, $\Delta H^\ddagger_6$ and $\Delta H^\ddagger_7$).

Table 2
Mechanistic modeling expressions for rate coefficients and equilibrium constants.

Rate coefficients, j = 4–7	$k_j = \exp\left[\frac{\Delta S^\ddagger_j}{R}\right] \exp\left[\frac{-\Delta H^\ddagger_j}{RT}\right]$
Equilibrium constants, j = 4–7	$k_j = \exp\left[\frac{\Delta S^\circ_j}{R}\right] \exp\left[\frac{-\Delta H^\circ_j}{RT}\right]$
Standard entropies of reaction	$\Delta S^\circ_4 = S^\circ_{H^*OH} - S^\circ_{H_2O} - S^\circ_*$
	$\Delta S^\circ_5 = S^\circ_{H_2} + S^\circ_{O^*} - S^\circ_{H^*OH}$
	$\Delta S^\circ_6 = S^\circ_{OCO^*} - S^\circ_{CO} - S^\circ_{O^*}$
	$\Delta S^\circ_7 = S^\circ_{CO_2} + S^\circ_* - S^\circ_{OCO^*}$
Standard enthalpies of reaction	$\Delta H^\circ_4 = \Delta H^\circ_{f,H^*OH} - \Delta H^\circ_{f,H_2O} - \Delta H^\circ_{f,*}$
	$\Delta H^\circ_5 = \Delta H^\circ_{f,H_2} + \Delta H^\circ_{f,O^*} - \Delta H^\circ_{f,H^*OH}$
	$\Delta H^\circ_6 = \Delta H^\circ_{f,OCO^*} - \Delta H^\circ_{f,CO} - \Delta H^\circ_{f,O^*}$
	$\Delta H^\circ_7 = \Delta H^\circ_{f,CO_2} + \Delta H^\circ_{f,*} - \Delta H^\circ_{f,OCO^*}$

$$H_2O + * \rightleftarrows H\text{–}*\text{–}OH \quad (4)$$

$$H\text{–}*\text{–}OH \rightleftarrows O\text{–}* + H_2 \quad (5)$$

$$CO + O\text{–}* \rightleftarrows OCO\text{–}* \quad (6)$$

$$OCO\text{–}* \rightleftarrows * + CO_2 \quad (7)$$

Modeling the experimental reactor as an isothermal, plug flow reactor led to five gas phase mole balances (four for the reagents plus one for any inert gas present, usually nitrogen or argon), three surface mole balances, and an equation for the conservation of active sites. These equations are given in Table 3 along with the initial conditions for the integration of the gas phase mole balances. These reactor design equations were solved numerically initially using an explicit Euler method, and later using an implicit Euler method. The integration step size was decreased until the solution converged to within less than 1%. Fitting the mechanistic models to the experimental data involved minimizing the sum of the squares of the differences between the measured CO conversion and that predicted by the mechanistic model. The Nelder-Mead simplex method [40] was used to do this, as described elsewhere [38].

3. Results and discussion

Before any experimental work began several different mechanistic models were fit to the experimental data published by Bohlbro for a ferrochrome high temperature shift catalyst. The Bohlbro data set consisted of 189 data points spanning a temperature range from 600 to 773 K, pressures from 1 to 20 atm and a variety of feed compositions. The merits of this data set have been considered previously [38], and it has already been demonstrated that a simple two-step microkinetic redox model fits the data set quite well. The problem with the two-step model used in the past is that it is highly unlikely that the steps involved could be elementary reactions. The mechanisms considered in the present work included carboxyl, carbonate, bicarbonate, and formate intermediates as well as simple redox processes. The number of mechanistic steps varied from 4 to 10. The four-step redox mechanism given in reactions (4)–(7) was found to fit the data as well as any of the mechanisms considered, and in addition, the three surface intermediates appearing in reactions (4)–(7) have been studied using computational chemistry.

Fig. 1 shows that the four-step redox model, reactions (4)–(7), fits the data well. The correlation coefficient, r^2, is equal to 0.92. For comparison purposes, a two-step redox model gave a correla-

Table 3
Reactor design equations.

Gas phase mole balances	$\frac{dn_{CO}}{dm} = -r_6$; $\frac{dn_{CO_2}}{dm} = r_7$; $\frac{dn_{H_2O}}{dm} = -r_4$; $\frac{dn_{H_2}}{dm} = r_5$; $\frac{dn_{inert\ diluent}}{dm} = 0$
Initial conditions	$n_{CO}(m=0) = n^\circ_{CO}$; $n_{H_2O}(m=0) = n^\circ_{H_2O}$; $n_{CO_2}(m=0) = n^\circ_{CO_2}$; $n_{H_2}(m=0) = n^\circ_{H_2}$; $n_{inert\ diluent}(m=0) = n^\circ_{inert\ diluent}$
Surface mole balances	$r_4 - r_5 = 0$; $r_5 - r_6 = 0$; $r_6 - r_7 = 0$
Conservation of active sites	$\theta_v + \theta_{HOH} + \theta_O + \theta_{OCO} = 1$

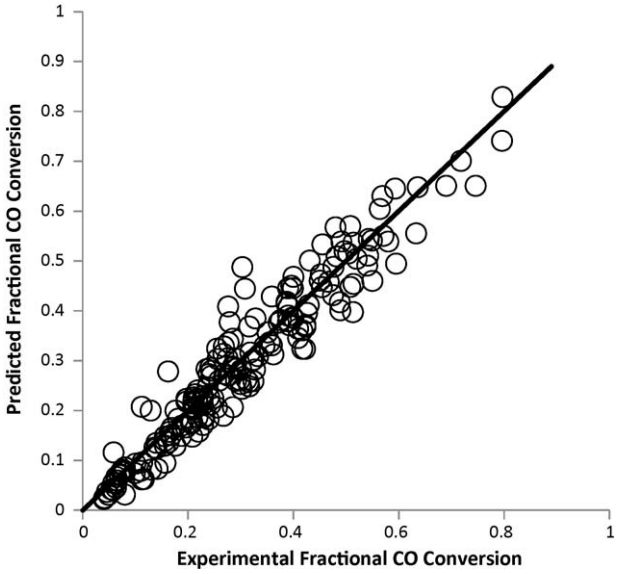

Fig. 1. Rectifying plot for the fit of the four-step mechanistic redox model to Bohlbro's data for an unpromoted ferrochrome catalyst.

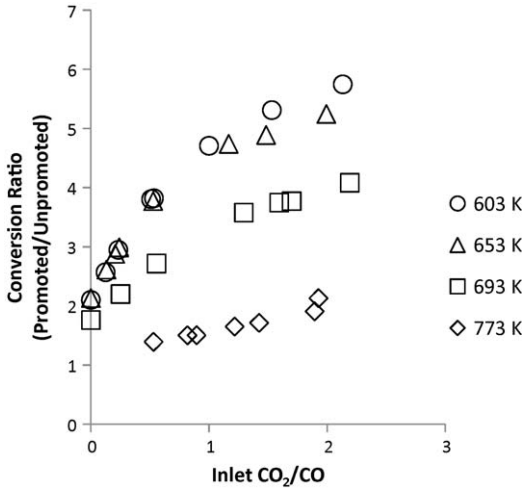

Fig. 2. CO conversion for copper-promoted ferrochrome relative to an unpromoted ferrochrome catalyst as predicted by the four-step mechanistic model. To predict conversions for a copper-promoted catalyst, the heats of localization of HOH and O from the unpromoted catalyst were decreased by 10 kJ mol^{-1}, as described in the text.

tion coefficient of 0.91 [38] and our fit of a power-law model gave 0.95. The corresponding parameter values are presented in Table 4. The hypersurface corresponding to the sum of the squares of the errors as a function of the unknown parameters had multiple local minima, and special effort was expended to attempt to identify all such local minima. The result reported in Table 4 corresponds to the smallest sum of the squares of the errors among the local minima. The existence of multiple local minima made it difficult to estimate the curvature matrix at the minimum point on the error hypersurface, which, in turn, made it difficult to assess the uncertainty in the resulting parameter values. Lacking such quantitative information, it can be noted qualitatively that the fit seemed most sensitive to the values of $\Delta H^{\circ}_{\mathrm{loc,HOH}}$, $\Delta H^{\circ}_{\mathrm{loc},0}$ and $\Delta H^{\ddagger}_{4}$, somewhat sensitive to $\Delta H^{\ddagger}_{5}$, and relatively insensitive to the remaining parameters.

Surface coverage can be computed using the mechanism, and doing so at 600 K indicates that 35% of the surface is covered by hydroxyl groups with the balance covered by oxygen. As the temperature is increased, the mechanism predicts decreasing hydroxyl concentration and increasing oxygen coverage so that at 800 K, hydroxyl groups cover only 2% of the surface sites, with the remainder being oxidized. The corresponding heat of dissociative adsorption of water at 298 K, reaction (4), is 182 kJ mol^{-1}. The variation in the coverage with temperature is consistent with direct experimental measurements [41,42]. The heat of adsorption resulting from the mechanistic model is significantly larger that derived from adsorption isotherms ($\geq$55 kJ mol^{-1}) [43], but it agrees very well with the result from computational chemistry (176 kJ mol^{-1}) [37].

Table 4
Mechanistic parameter sets resulting from kinetic modeling.

Parameter	Bohlbro's ferrochrome catalyst (kJ mol^{-1})	Copper-promoted (5 wt.%) catalyst (kJ mol^{-1})
$\Delta H^{\circ}_{\mathrm{loc,HOH}}$	−681	−661
$\Delta H^{\circ}_{\mathrm{loc,O}}$	−599	−568
$\Delta H^{\circ}_{\mathrm{loc,OCO}}$	−1.2	−176
$\Delta H^{\ddagger}_{4}$	24.2	0
$\Delta H^{\ddagger}_{5}$	93.4	76.6
$\Delta H^{\ddagger}_{6}$	0.8	66.5
$\Delta H^{\ddagger}_{7}$	0	0
Correlation coefficient, r^2	0.92	0.88

There is spectroscopic and chemical trapping evidence for the presence of surface carbonate, carboxylate and formate intermediates as well. The heat of CO_2 adsorption at 298 K (i.e. the reverse of reaction (7)) predicted by mechanistic kinetic modeling is only 1.2 kJ mol^{-1}. Experimental measurements of this quantity by Kwan and Fujita [44] and Udovic and Dumesic [45] gave values of 44 and 50–60 kJ mol^{-1}, respectively (using the unidentate value in the latter case). However, as already noted, the fit of the mechanistic model was not sensitive to the heat of localization of CO_2. For example, the heat of localization of CO_2 could be decreased by 60 kJ mol^{-1}, putting it in the range of the reported experimental values, and the sum of the squares of the errors for the fit only changed by 15% and the correlation coefficient (r^2) remained equal to 0.92. In contrast, changing either the heat of localization of dissociated water or that of oxygen by the much smaller amount of only 10 kJ mol^{-1} caused the sum of the squares of the errors to change by 200% while r^2 decreased to 0.85 and 0.87, respectively.

The mechanistic model was next used to predict how substitution of sub-surface copper cations in place of iron cations would affect the catalyst's performance. Recall, computational chemistry suggests that sub-surface copper substitution decreases the heats of localization by 10–20 kJ mol^{-1}. Accordingly, the heats of localization of dissociated water and of oxygen were both decreased by 10 kJ mol^{-1}. Decreasing the heat of localization of carbon dioxide by this amount would result in a negative heat of adsorption, so in light of the insensitivity of the model to this parameter, the heat of localization of carbon dioxide was not changed. In this way the predicted catalytic performance of a copper-promoted catalyst was compared to the performance of an unpromoted ferrochrome. The results are shown in Fig. 2.

Fig. 2 predicts two consequences of sub-surface copper promotion. First, it predicts that sub-surface copper cation substitution leads to increased activity at lower temperatures, but not at higher temperatures. This can be seen by noting that the CO conversion ratio (promoted over unpromoted) is much higher than unity at low temperatures, but it approaches unity as the temperature increases. This is consistent with the literature cited in Section 1. Second, the model suggests that sub-surface copper promotion lessens the inhibition of the forward rate by CO_2. This can be seen in the figure by noting that as the inlet CO_2/CO ratio increases, the conversion ratio (promoted over unpromoted) also increases. The latter prediction was tested experimentally as discussed presently.

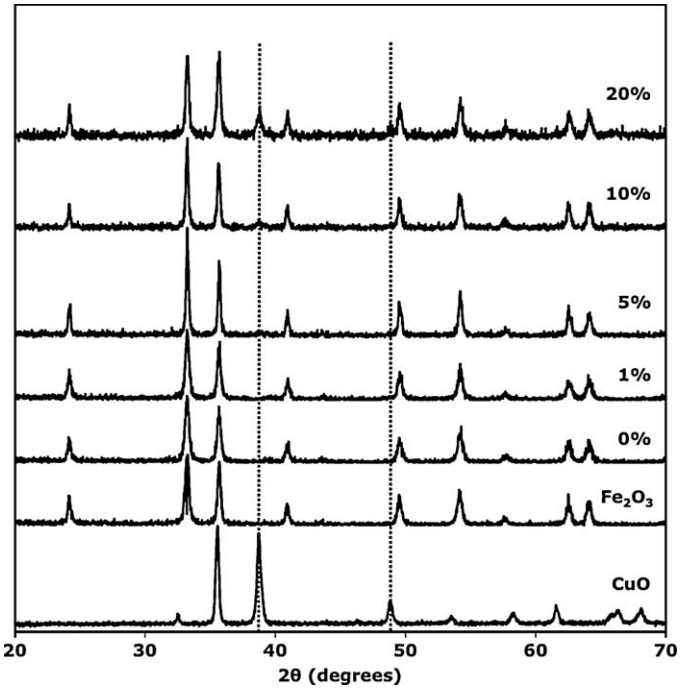

Fig. 3. XRD patterns showing that in the as-prepared, copper-promoted catalysts the iron oxide is present as Fe_2O_3 and the copper, when detected, is present as CuO. Dashed lines indicate the strongest copper oxide peaks that do no overlap with iron oxide peaks.

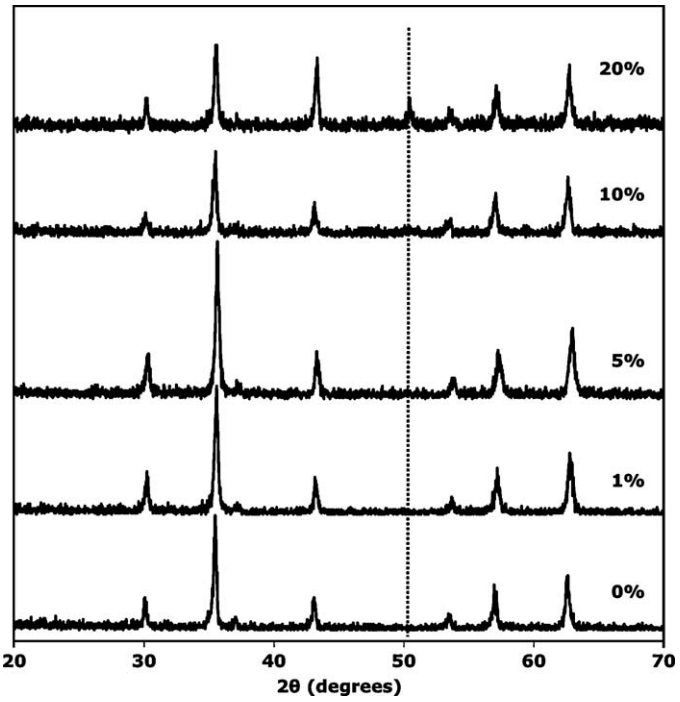

Fig. 4. XRD patterns showing that after use in water-gas shift, the iron oxide is in the catalysts is present as Fe_3O_4 and the copper, when detected, is present as metallic copper. The dashed line indicates the strongest line for metallic copper that does not overlap with iron oxide peaks.

Powder X-ray diffraction (XRD) patterns for the as-prepared series of copper catalysts are shown in Fig. 3. Corresponding XRD patterns for the same materials after use as water-gas shift catalysts are shown in Fig. 4, and changes in the BET surface area are listed in Table 5, which also reports the measured copper contents of the catalysts. The used samples in Fig. 4 and Table 5 had been under shift reaction conditions for varying lengths of time (several days to weeks) during which kinetic data were gathered. At the higher loadings of copper, both the as-prepared catalysts and the used catalysts show XRD peaks that can be attributed to a separate copper or copper oxide phase (see the dashed lines in the figures). This might be expected if the copper substitution into the iron oxide lattice approaches saturation as the loading increases, causing a separate copper-containing phase to form. It is possible that a separate copper-containing phase also exists at the lower loading, but that the particles are too small to be detected using XRD. The XRD data also evidence the expected transformation of the Fe_2O_3 structure observed in the as-prepared materials to the Fe_3O_4 structure seen in the used catalysts. Table 5 shows that while the surface area decreases with increasing copper loading, the surface area at each catalyst loading was stable, within the uncertainty of the measurement, over the period of catalytic testing.

The XRD data for the used catalyst suggest that metallic copper particles are indeed present on the catalyst surface at working conditions, as previously reported by others [34,35]. It is likely that the catalysts also have copper cations substituted within the oxide. The key question is whether the promotional effect of copper can be attributed to one or the other of these forms of copper. Sub-surface substitution was predicted to cause a significant decrease in the inhibition by CO_2, as discussed for Fig. 2. In contrast, for metallic copper the inhibition by CO_2 is expected to be nearly the same as that for ferrochrome (Bohlbro [1] found the CO_2 order to equal −0.6 for ferrochrome and Gokhale et al. [36] report it to equal −0.5).

The apparent CO_2 reaction order was measured for the series of copper-promoted catalysts of varying loading. The results shown in Fig. 5 indicate that a copper loading of the order of 5–10 wt% optimizes the catalyst performance. At these loadings, it was possible to detect metallic copper particles on the catalyst (Fig. 4), but the corresponding reaction order in CO_2 (−0.26) is smaller than expected for metallic copper (−0.5). This favors a cation substitution model for promotion, but given the uncertainty in the measured orders, an unequivocal conclusion is not possible. Even if metallic copper particles are not responsible for decreasing the inhibition by CO_2, they could still play a role in mitigation of methane formation at low steam to carbon monoxide feed ratios.

A mechanistic kinetics study was performed using the ferrochrome catalyst promoted with 5 wt% copper. The 57 data points spanned a temperature range from 658 to 756 K, pressures from 1

Table 5
BET surface area of fresh/used copper-promoted ferrochrome catalysts.

Catalyst	Metal weight percentages Fe/Cr/Cu	Fresh BET surface area (m^2/g cat)	Used BET surface area (m^2/g cat)
FeCr10	59.47/5.84/0	39.6	38.0
0.1%CuFeCr10	59.40/5.95/0.13	34	31.6
1%CuFeCr10	59.46/5.72/0.91	26.7	27.6
5%CuFeCr10	56.52/5.50/4.20	26.1	25.2
10%CuFeCr10	–	16.7	20.5
20%CuFeCr10	–	14.6	17.0
Fe_2O_3	–	37.2	13.6
CuO	–	0.584	–

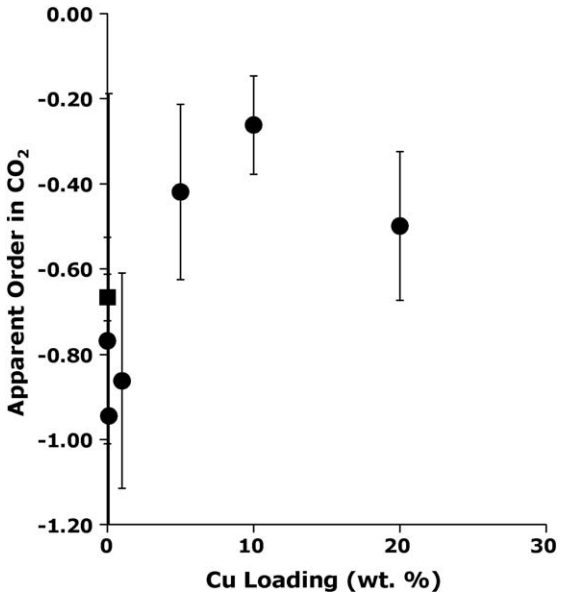

Fig. 5. Apparent CO_2 reaction order as a function of copper loading of the copper-promoted ferrochrome catalysts listed in Table 5.

to 3 atm, H_2O/CO ratios from 1 to 6.2, CO_2/CO ratios from 0 to 6.7 and H_2/CO ratios from 0 to 1.0. The four-step mechanistic model (Eqs. (4)–(7)) was fit to the resulting kinetic data. The best parameter set resulting from the fit is presented in Table 4. Fig. 6 shows that the four-step redox model fits the data for the promoted catalyst reasonably well. The correlation coefficient (r^2) was equal to 0.88. The heats of localization for dissociated water and for oxygen for the copper-promoted catalyst were smaller than the corresponding values for Bohlbro's catalyst by ca. 20 and 30 kJ mol^{-1}, respectively. This finding is very close to that predicted by computational chemistry. The heats of localization of carbon dioxide differ substantially, but it has already been noted that the fit of model for the unpromoted catalyst was insensitive to this parameter.

Three of the four activation enthalpies also change by ca. 20 and 30 kJ mol^{-1}. No other experimental or computational data are available for comparison, but changes of this order of magnitude might be expected. Correlation is often observed between the heat of reaction and the activation energy. In contrast, the activation energy for step (6) for the copper-promoted catalyst is significantly greater than that found for the unpromoted catalyst. Additional study will be required to reveal the reason for this larger change in activation energy.

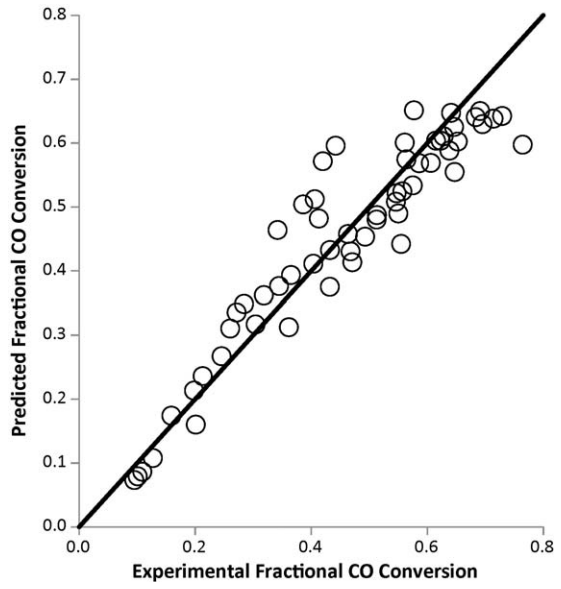

Fig. 6. Rectifying plot for the fit of the four-step mechanistic redox model to kinetic data for the 5 wt.% copper-promoted ferrochrome catalyst (5%CuFeCr10).

The present results should not be taken to support the redox mechanism for water-gas shift over associative mechanisms. An associative mechanism involving a formate intermediate was formulated by replacing reactions (5) and (6) with reactions (8) and (9). The resulting four-step associative mechanism was fit to Bohlbro's ferrochrome data and the present copper-promoted ferrochrome data. Statistically, the fits for the associative mechanism were as good as those for the redox mechanism (r^2 = 0.92 in both cases for the ferrochrome catalyst and r^2 = 0.88 in both cases for the copper-promoted catalyst). The differences in the associative mechanism heats of localization for H_2O, HCOOH and CO_2 between the unpromoted and the copper-promoted catalysts were 65, 54 and 5 kJ mol^{-1}, respectively. While these changes are greater than those for the redox mechanism, they are still within the range predicted by DFT calculations when copper cations replace iron cations in the surface of Fe_3O_4.

$$CO + H\text{–}^*\text{–}OH \rightleftarrows H\text{–}^*\text{–}COOH \quad (8)$$

$$H\text{–}^*\text{–}COOH \rightleftarrows OCO\text{–}^* + H_2 \quad (9)$$

As noted in Section 1, two explanations have been offered regarding the role of copper as a promoter: that the promotional effect is a result of copper cation substitution within the iron oxide and that it is a result of the formation of metallic copper nanoparticles. One might expect that if the promotional effects are due to metallic copper nanoparticles that form under reaction conditions, then the mechanism of water-gas shift for a promoted catalyst would be different from that for an unpromoted catalyst. While the present results do not discriminate between redox and associative mechanisms, they do show that in either case, the *same* mechanism can describe the kinetics of both the unpromoted and the copper-promoted catalyst. Furthermore, they show that the changes in the thermodynamic parameters that are necessary in order to fit both data sets are within the range predicted by DFT calculations on the substitution of copper cations for iron cations in the iron oxide catalyst. Thus, it is not necessary that metallic copper be present in order to explain the *kinetics* of a copper-promoted water-gas shift catalyst. If, in fact, metallic copper nanoparticles *are* the active entity in copper-promoted catalysts, it would seem to be highly coincidental that (a) the mechanism can remain unchanged and (b) the thermodynamic parameters derived from the mechanism are so similar to those for an iron oxide catalyst.

4. Conclusions

The four-step redox mechanism given in Eqs. (4)–(7) described the rate of water-gas shift measured by Bohlbro over a ferrochrome catalyst. The resulting model also predicted variations in surface coverage that were consistent with literature reports. However, the heats of adsorption of water and carbon dioxide resulting from the kinetic modeling differed from reported isosteric heats of adsorption.

When copper was added to a ferrochrome catalyst as a promoter, the same four-step redox mechanism described the experimentally measured rate of water-gas shift, though there were some differences in the values of the thermodynamic parameters appearing in the mechanistic model. The degree of inhibition of the water-gas shift rate by carbon dioxide decreased as the copper loading increased. Metallic copper was detected in the catalyst samples following their use.

The mechanistic kinetic similarities between ferrochrome and copper-promoted ferrochrome strongly suggest that the active sites on the two catalysts are similar. This is also true when an associative water-gas shift mechanism is used. This favors copper ions substituted within the iron oxide over separate metallic copper particles as the source of the changes in catalytic activity. However, while some of the thermodynamic parameters appearing in the mechanistic kinetic models are consistent with independent measurement or calculation, others are not. As such, it is not possible, on the basis of the mechanistic modeling, to conclude definitively which form of copper causes the catalytic promotion.

Acknowledgements

Acknowledgement is made to the Donors of the American Chemical Society Petroleum Research Fund for support of this research. The experimental assistance of Mr. Jason Greene is also acknowledged.

References

[1] H. Bohlbro, An Investigation on the Conversion of Carbon Monoxide with Water Vapour over Iron Oxide based Catalysts, Haldor Topsøe, Gjellerup, Copenhagen, 1969.
[2] H. Bohlbro, Acta Chem. Scand. 15 (1961) 502.
[3] H. Bohlbro, Acta Chem. Scand. 16 (1962) 431.
[4] H. Bohlbro, Acta Chem. Scand. 17 (1963) 1001.
[5] H. Bohlbro, J. Catal. 3 (1964) 207.
[6] H. Bohlbro, M.H. Jorgensen, Chem. Eng. World 5 (1970) 46.
[7] O. Stelling, O. von Krusentierna, Acta Chem. Scand. 12 (1958) 1095.
[8] C. Rhodes, G.J. Hutchings, A.M. Ward, Catal. Today 23 (1995) 43.
[9] E.F. Armstrong, T.P. Hilditch, Proc. Roy. Soc. Lond. 97A (1920) 265.
[10] G.K. Boreskov, Kinet. Catal. 11 (1970) 312.
[11] G.K. Boreskov, T.M. Yur'eva, A.S. Sergeeva, Kinet. Catal. 11 (1970) 1230.
[12] C. Diagne, P.J. Vos, A. Kiennemann, M.J. Perrez, M.F. Portela, React. Kinet. Catal. Lett. 42 (1990) 25.
[13] J.E. Kubsh, J.A. Dumesic, AIChE J. 28 (1982) 793.
[14] C.R.F. Lund, J.A. Dumesic, J. Catal. 76 (1982) 93.
[15] C.R.F. Lund, J.A. Dumesic, ACS Meeting, Miami Beach, 1985.
[16] G.G. Shchbrya, N.M. Morozov, M.I. Temkin, Kinet. Catal. 6 (1965) 955.
[17] S. Oki, Y. Kaneko, ACS Conference, Hawaii, 1979.
[18] S. Oki, R. Mezaki, J. Phys. Chem. 77 (1973) 447.
[19] S. Oki, R. Mezaki, J. Phys. Chem. 77 (1973) 1601.
[20] N.A. Rubene, A.A. Davydov, A.V. Kravtsov, N.V. Usheva, S.I. Smol'yaninov, Kinet. Katal. 17 (1976) 465.
[21] A.M. Alekseev, I.P. Kirillov, V.V. Kostrov, Izvestiya Vysshikh Uchebnykh Zavedenii, Khim. Khim. Tekhnol. 10 (1967) 308.
[22] F. Domka, A. Basinska, R. Fiedorow, Surf. Technol. 18 (1983) 275.
[23] F. Domka, A. Basinska, W. Przystajko, R. Fiedorow, Surf. Technol. 21 (1984) 101.
[24] M.A. Edwards, D.M. Whittle, C. Rhodes, A.M. Ward, D. Rohan, M.D. Shannon, G.J. Hutchings, C.J. Kiely, Phys. Chem. Chem. Phys. 4 (2002) 3902.
[25] M.I. Markina, G.K. Boreskov, F.P. Ivanovskii, B.G. Lyudkovskaya, Kinet. Katal. 2 (1961) 867.
[26] J.H. Carstensen, J.B. Hansen, P.S. Pedersen, Ammonia Plant Safety & Related Facilities, vol. 30, 1990, p. 139.
[27] C. Rhodes, G.J. Hutchings, Phys. Chem. Chem. Phys. 5 (2003) 2719.
[28] A. Andreev, V. Idakiev, D. Mihajlova, D. Shopov, Appl. Catal. 22 (1986) 385.
[29] C. Rhodes, B.P. Williams, F. King, G.J. Hutchings, Catal. Commun. 3 (2002) 381.
[30] L. Zhang, J.M. Millet, U.S. Ozkan, Appl. Catal. A: Gen. 357 (2009) 66.
[31] L. Zhang, X. Wang, J.M. Millet, P.H. Matter, U.S. Ozkan, Appl. Catal. A: Gen. 351 (2008) 1.
[32] V. Idakiev, D. Mihailova, B. Kunev, A. Andreev, React. Kinet. Catal. Lett. 33 (1987) 119.
[33] P. Kappen, J.-D. Grunwaldt, B.S. Clausen, J. Catal. 198 (2001) 56.
[34] J.-D. Grunwaldt, B.S. Clausen, Top. Catal. 18 (2002) 37.
[35] J.D. Grunwaldt, P. Kappen, B.S. Hammershoi, L. Troger, B.S. Clausen, J. Synchrotron Radiat. 8 (2001) 572.
[36] A.A. Gokhale, J.A. Dumesic, M. Mavrikakis, J. Am. Chem. Soc. 130 (2008) 1402.
[37] R.M. Van Natter, J.S. Coleman, C.R.F. Lund, J. Mol. Catal. A: Chem. 311 (2009) 17.
[38] R.M. Van Natter, J.S. Coleman, C.R.F. Lund, J. Mol. Catal. A: Chem. 292 (2008) 76.
[39] NIST Chemistry WebBook, National Institute of Standards and Technology, Gaithersburg, MD 20899, 2005, NIST Standard Reference Database Number 69 http://webbook.nist.gov.
[40] J.A. Nelder, R. Mead, Comput. J. 7 (1965) 308.
[41] T. Morimoto, M. Nagao, F. Tokuda, J. Phys. Chem. 73 (1969) 243.
[42] T. Morimoto, Y. Yokota, M. Nagao, J. Colloid Interface Sci. 64 (1978) 188.
[43] Y. Joseph, C. Kuhrs, W. Ranke, W. Weiss, Surf. Sci. 433–435 (1999) 114.
[44] T. Kwan, Y. Fujita, J. Res. Inst. Catal. Hokkaido Univ. 2 (1953) 110.
[45] T.J. Udovic, J.A. Dumesic, J. Catal. 89 (1984) 314.